Covalent organic frameworks as catalyst support: A case study of thermal, hydrothermal, and mechanical pressure stability of β-ketoenamine-linked TpBD-Me₂

Liliana P.L. Gonçalves [a,b,c], Javier Garcia Ben [a,d], Karol Strutyński [e], Laura Rodriguez-Lorenzo [a], Joana Araújo [a], A.Sofia G.G. Santos [b,c], O. Salomé G.P. Soares [b,c], M. Fernando R. Pereira [b,c,****], Yury V. Kolen'ko [a,***], Manuel Melle-Franco [e,**], Laura M. Salonen [f,a,*]

[a] International Iberian Nanotechnology Laboratory, Avenida Mestre José Veiga s/n, 4715-330, Braga, Portugal
[b] LSRE-LCM - Laboratory of Separation and Reaction Engineering – Laboratory of Catalysis and Materials, Faculty of Engineering, University of Porto, Rua Dr. Roberto Frias, 4200-465, Porto, Portugal
[c] ALiCE - Associate Laboratory in Chemical Engineering, Faculty of Engineering, University of Porto, Rua Dr. Roberto Frias, 4200-465, Porto, Portugal
[d] Universidade da Coruña, Quimolmat, CICA - Centro Interdisciplinar de Química e Bioloxía, Rúa as Carballeiras, 15071, A Coruña, Spain
[e] CICECO—Aveiro Institute of Materials, Department of Chemistry, University of Aveiro, 3810-193, Aveiro, Portugal
[f] CINBIO, Universidade de Vigo, Department of Organic Chemistry, 36310, Vigo, Spain

ARTICLE INFO

ABSTRACT

Covalent organic frameworks (COFs) are crystalline, ordered networks, that, due to their high surface areas and the opportunity for periodic placement of catalytically active sites, are interesting materials for catalysis. Despite the great interest in the use of COFs for this application, there is currently a lack of fundamental understanding on how catalytically relevant conditions affect the integrity of the materials. To gain insight into the stability of COFs as catalyst supports, we herein subjected a β-ketoenamine-linked COF to thermal treatment at high temperatures, to autogenous pressure in water at different temperatures, and to mechanical pressure during pelletizing, after which the materials were thoroughly characterized to gain insight into the structural changes occurring during these catalytically relevant treatments. The COF was largely stable under all hydrothermal conditions studied, highlighting the applicability of β-ketoenamine-linked COFs under aqueous and vapor conditions. On the other hand, thermal and pressure treatments led to a rapid decline in the surface area already at the lowest temperatures and pressures studied. Theoretical calculations indicated this loss to stem from interlayer rearrangement or buckling of the COF layers induced by the applied conditions. This study demonstrates the suitability of β-ketoenamine-linked COFs for use under hydrothermal conditions, and sheds light on the degradation pathways under thermal and pressure treatments, opening the path to the design of COFs with increased stability under such conditions.

1. Introduction

Catalysis holds a key position in chemical production, and therefore, the development of improved catalysts is fundamental for the current and emerging industrial processes. In addition to tailoring the active phase of a catalyst, to increase its activity and durability, catalyst supporting materials are often used to achieve a high-performing catalyst [1]. Important features of the supporting material are the accessibility of coordination sites for the deposition of the catalytically active metal atoms, nanoclusters, or nanoparticles (NPs), allowing for a good

* Corresponding author. CINBIO, Universidade de Vigo, Department of Organic Chemistry, 36310, Vigo, Spain.
** Corresponding author. CICECO—Aveiro Institute of Materials, Department of Chemistry, University of Aveiro, 3810-193, Aveiro, Portugal.
*** Corresponding author.
**** Corresponding author. LSRE-LCM - Laboratory of Separation and Reaction Engineering – Laboratory of Catalysis and Materials, Faculty of Engineering, University of Porto, Rua Dr. Roberto Frias, 4200-465, Porto, Portugal.
E-mail addresses: fpereira@fe.up.pt (M.F.R. Pereira), yury.kolenko@inl.int (Y.V. Kolen'ko), manuelmelle@gmail.com (M. Melle-Franco), lauramaria.salonen@uvigo.es (L.M. Salonen).

distribution of active sites throughout the material and high surface area, facilitating access of the reactants to the active sites.

Two-dimensional (2D) covalent organic frameworks (COFs) are crystalline porous materials, in which organic building blocks are connected via covalent bonds to form sheets that stack in the third dimension to form a porous structure [2–5]. These materials enable the integration of the building blocks into an ordered structure with atomic precision, affording the creation of predesigned skeletons and nanopores, and the periodic placement of catalytically active sites through the catalyst [6]. Their covalent-bonding architecture provides them with unique properties, such as low mass densities, high thermal and chemical stabilities, and large surface area [7–9]. Hence, COFs are being actively explored for catalysis, either as catalysts or as catalyst supporting materials[10–17] complementary to metal oxides, high-surface-area silicas, and carbon-based materials.

In the first example of the use of a COF as catalyst support, Wang and co-workers [7] showed Pd/COF-LZU1 to feature excellent catalytic activity for Suzuki−Miyaura cross-coupling reaction, with the metal sites incorporated between the COF layers and the regular channels providing efficient access to the active sites and fast diffusion of the products. Thereafter, studies on COFs as catalysts for a wide variety of transformations have emerged [12,18–21]. We previously prepared a pre-catalyst consisting of RuO_2 NPs and nanoclusters supported on TpBD-Me$_2$ [8]. This COF, first reported by Banerjee and co-workers [22], is a highly hydrolytically stable 2D β-ketoenamine-linked COF, which can be synthesized on a gram scale [8,23], crucial for application as catalyst support. The defined porosity of the COF afforded the precipitation of well-dispersed RuO_2 NPs together with small RuO_2 nanoclusters and single Ru atoms. Under formic acid dehydrogenation conditions, RuO_2 in our TpBD-Me$_2$ catalyst was reduced *in situ* to metallic Ru, and the material featured excellent activity and selectivity, outperforming a commercial Ru/C catalyst.

Although the chemical structure of the TpBD-Me$_2$ COF support was maintained during stability testing, as confirmed by Fourier-transform infrared spectroscopy (FTIR), the crystallinity of the material was found to decrease under the reaction conditions. Intrigued by this finding, we wanted to gain more insight into the structural and textural changes occurring under catalytically relevant conditions. Most catalytic applications require the use of elevated temperatures and pressures, and therefore, it is of high importance to assess the stability of the catalytic materials under such conditions, as well as to understand the degradation pathways to assist in the design of durable catalysts. To the best of our knowledge, despite the intensive exploration of COFs for catalysis [10–16], their stability has not yet been assessed in a systematic manner with a focus on conditions pertinent to catalysis.

Herein, we address this gap by systematically studying the stability of β-ketoenamine-linked TpBD-Me$_2$ under catalytically relevant conditions. The material was subjected to high temperatures and to autogenous pressure in water at different temperatures, as common in heterogeneous catalysis, and to mechanical pressure during pelletizing, shaping being an important step in catalytic applications. Full characterization of the COF before and after these treatments coupled to theoretical calculations gave insight into the structural changes occurring in the material during the treatments, and provided indications on the future optimization of COF structures for catalytic application.

2. Material and methods

2.1. Stability evaluation

To assess the stability of TpBD-Me$_2$ [23,24], the COF was subjected to different conditions. Specifically, to evaluate the thermal stability of TpBD-Me$_2$, 150 mg of the material was placed in alumina crucible, in a tubular furnace and the temperature was increased to 150, 200, and 250 °C at 10 °C min^{-1} under N$_2$ flow rate of 100 cm^3 min^{-1}, and left at the corresponding temperature for 1 h.

For the evaluation of hydrothermal stability, TpBD-Me$_2$ (150 mg) was placed in a Teflon container along with 40 mL of ultrapure water and inserted into a stainless-steel autoclave that was heat treated at 100, 150, and 200 °C for 24 h. The material was then collected by filtration and dried under vacuum at 120 °C.

Finally, the stability of TpBD-Me$_2$ under mechanical pressure was assessed by exerting different mechanical pressures to the COF with a hydraulic press. The sample was subjected to 1, 3, and 5 ton for 10 min, which correspond to a pressure of 75, 225, and 375 MPa, respectively, taking into account the area of the pellet form with diameter of 13 mm. The pellets were then broken into smaller pieces before characterization, and they were ground into a fine powder for the SAXS measurements.

2.1.1. Characterization

Powder X-ray diffraction (XRD) analyses were performed on an X'Pert PRO MRD diffractometer (PANalytical) operated at 45 kV and 40 mA.

The crystallinity of the material was investigated by means of small-angle X-ray scattering (SAXS) performed on a SAXSess mc^2 instrument (Anton Paar) operated at 40 kV and 50 mA. The samples were placed into a holder with Mylar windows for the measurement, and the data was collected with an image plate detector. All data are background corrected. The degree of crystallinity of the COF can be estimated by analyzing the width of the Bragg peaks, which is dependent on the domain size of the structure (i.e., the length over which the structure is coherent). To eliminate the background caused by the overlapping of the Bragg peak of the sample with the scattering from other structural features, the Bragg peak was approximated by a Lorentzian function of the following type:

$$I(q) = \frac{A}{w^2 + (q - q_0)^2} \tag{1}$$

where $I(q)$ is the q-dependent scattered intensity, A is the amplitude of the peak, w is the half-width at half-maximum (HWHM) of the peak, q is the scattering vector, and q_0 is the q position of the peak maximum. Normalizing the scattering intensity by the maximum intensity of the peak, the normalized function is

$$I(q) = \frac{A}{w^2 + (q - q_0)^2} + Bq^2 + Cq + D \tag{2}$$

where B, C, and D are the polynomial coefficients. The domain size (L) of the sample can be given by

$$L = \frac{\pi}{w} \tag{3}$$

The N$_2$ adsorption−desorption isotherms at 77 K were recorded using an Autosorb IQ^2 multi-station apparatus (Quantachrome). Approximately 50 mg of sample was placed in the sample holder tube. The sample was degassed at 120 °C for 12 h. After that, the sample holder tube was placed into a liquid nitrogen bath for the analysis. The specific surface area (S_{BET}) of the materials was determined by the Brunauer−Emmett−Teller (BET) method, and the total pore volume (V_P) was calculated using the amount of vapor adsorbed at relative pressure close to unity ($P/P_0 = 0.97$) by assuming that the pores were filled with liquid adsorbate, and thus, converting the adsorbed volume in volume of liquid nitrogen. The pore size distribution was estimated using quenched-solid density functional theory approach for slit/cylindrical pores treating the adsorption branch of the isotherm.

Fourier-transform infrared (FTIR) spectra were acquired on a VERTEX 80v FT-IR spectrometer (Bruker) in attenuated total reflectance (ATR) mode. A spatula tip of the sample was used without further treatment. Spectra were recorded at 1.66 hPa with 32 scans and 4 cm^{-1} resolution with a mercury−cadmium−telluride (MCT) detector. The empty holder at 1.66 hPa was used as background, and baseline correction was applied to the collected spectra.

Raman spectroscopy specimens from TpBD-Me$_2$ powder were prepared by pressing 2–3 mg of powder between two glass slides. The resultant flat specimens were analyzed by Raman spectroscopy upon excitation with a 785 nm laser line, using a 300R confocal Raman microscope (Witec) with a high-resolution diffraction grating (600 gr mm^{-1}), and a Peltier-cooled CCD detector (-70 °C). Raman spectroscopy mapping was carried out within the 150–1900 cm^{-1} range and in areas of 100×100 µm, with a step size of 2 µm, accumulation time of 1 s, and laser power at the sample of 5 mW. The laser was focused on the flat specimen by using a $50 \times$ objective (N.A. 0.55) providing a laser spot size of about 2 µm. Data processing was performed with Project 5.1 software package (WITec). Raman spectroscopy mappings were obtained based on the full width at half maximum (FWHM) of the Raman peak centered at 1607 cm^{-1}, one of the characteristic peaks of TpBD-Me$_2$.

Thermogravimetric analysis (TGA) was performed in a TGA/DSC 1 STAR equipment (Mettler-Toledo), by heating the sample under Ar flow of 30 cm^3 min^{-1} from 50 to 900 °C, at a heating rate of 10 °C min^{-1}.

Scanning electron microscope (SEM) images were acquired on FEI Quanta 650 FEG under high vacuum through an Everhart-Thornley detector (ETD), with an acceleration voltage of 15.00 kV at a working distance of 10 mm, 30000× magnification and a beam spot size of 3.0.

X-ray photoelectron spectroscopy (XPS) measurements were performed using a monochromated microfocused Al Kα X-ray source that defined an analysis spot of ca. 650×400 µm^2. Powdered samples were pressed onto a carbon tape, which was directly attached to the sample holder.

Charge neutralization was provided by "in-lens" flood gun. A convolution of Lorentzian and Gaussian lineshapes on a linear combination of Shirley and linear backgrounds was used to fit the individual components, choosing the minimal number of self-consistent components that were able to fit spectra across all the samples. The number of components for C 1s, N 1s, and O 1s spectra was fixed based on the fits for the pristine COF sample. Binding energies were calibrated relative to the C 1s peak for aliphatic and aromatic carbon at 284.5 eV.

2.2. Computational modelling

The GFN1-xTB Hamiltonian [25] within the DFTB module of the Amsterdam Modeling Suite [26] was used for Molecular Dynamics (MD). Preliminary structure optimization was performed with 3OB [27] Hamiltonian with D4 van der Waals corrections [28] using the DFTB + program [29]. All DFT calculations were performed with the Fritz Haber Institute *ab initio* molecular simulations (FHI-aims) package [30–32] [30–32] [30–32] using "light" numeric atomic orbitals, which approximately correspond to TZVP level of calculations. The PBE functional augmented with Many Body Dispersion corrections [33,34] was used for geometry optimization and energies. The Γ-centered $3 \times 3 \times 1$ *k*-point grid was utilized for monolayer and $3 \times 3 \times 2$ for multilayer calculations. The PoreBlazer v4.0 program [35,36] was used to compute the porosity of the simulated structures with a virtual nitrogen molecule.

2.3. Catalytic testing

The as-synthesized TpBD-Me$_2$ COF as well as the material after thermal treatment at 200 °C, after hydrothermal treatment at 200 °C, and pressure treatment at 375 MPa were tested for catalytic BrO$_3^-$ reduction as a model reaction in a semi-batch reactor (ca. 1 L). In a typical run, 25 mg of the catalyst was added to the reactor containing 197.5 mL of ultrapure water. A pre-reduction step of the catalyst was performed for 15 min, where the solution inside of the reactor, along with the catalyst, was in contact with H$_2$ (25 cm^{-3} min^{-1}) that was continuously fed to the reactor, under a stirring rate of 400 rpm. After the pre-reduction period, 2.5 mL of a concentrated BrO$_3^-$ solution (prepared from NaBrO$_3$) was added to the reactor to obtain an initial BrO$_3^-$ concentration of 200 µg L^{-1}.

Small samples were taken from the reactor with a syringe to determine BrO$_3^-$ degradation over time, after defined times, during a 3 h period. The BrO$_3^-$ reduction progress was followed using a Shimadzu Bromate Analysis LC system, with a post-column reaction, using an aqueous solution of 12 mM NaHCO$_3$ and 0.6 mM Na$_2$CO$_3$ mobile phase for bromate separation, and a 1.5 M KBr, 1 M H$_2$SO$_4$, and 1.2 mM NaNO$_2$ aqueous solution for post-column reaction for UV detection at 268 nm.

3. Results

3.1. Treatment under catalytically relevant conditions

TpBD-Me$_2$ (Fig. 1a) was prepared using a procedure developed by our group, which gives access to the COF in 2 g scale (see Supplementary Data (SD) for details) [23]. To study the stability of TpBD-Me$_2$ under catalytically relevant conditions, the material was subjected to different temperatures under inert atmosphere and in water, as well as mechanical pressure. Thermal treatments were performed under inert atmosphere to avoid possible burning of COF due to the presence of O$_2$ at high temperatures. The thermal stability (T) of TpBD-Me$_2$ was determined by treating the material at 150, 200, and 250 °C at 10 °C min^{-1} under N$_2$. To this end, the sample was placed in a crucible in a tubular furnace and the temperature was increased under N$_2$ flow and maintained at the corresponding temperature for 1 h. For the evaluation of hydrothermal stability (HT), TpBD-Me$_2$ was subjected to 100, 150, and 200 °C in water at autogenous pressure, typical conditions in many catalytic applications. The material was placed in a Teflon container with ultrapure water and inserted into a stainless-steel autoclave that was heated in an oven at the selected temperatures for 24 h. After that, the material was filtered and dried under vacuum. Pelletizing is an important step in catalytic applications [37], and it is usually carried out by exerting mechanical pressure on the catalytic materials. Therefore, the stability of TpBD-Me$_2$ under mechanical pressure (P) was assessed by exerting different pressures on the material, namely, 75, 225, and 375 MPa with a mechanical press for 10 min, in a form with a diameter of 13 mm.

3.2. TpBD-Me$_2$ characterization after treatment

To obtain a comprehensive understanding of the stability of TpBD-Me$_2$ (Fig. 1a) when subjected to T, HT, and P treatments, we analyzed the changes in the crystallinity, textural properties, and chemical structure of the material after treatment using small-angle X-ray scattering (SAXS), N$_2$ physisorption [Brunauer–Emmett–Teller surface area (S_{BET}), pore size (d_P), total pore volume (V_P), micropore volume (V_{micro})], as well as FTIR and Raman spectroscopies, and compared the results with the pristine material.

The powder X-ray diffraction (XRD) pattern (Fig. 1b) of the pristine TpBD-Me$_2$ features three reflections: one at $2\theta \approx 3.4°$ (i.e., $q \approx 2.4$ nm^{-1} in the SAXS pattern), corresponding to the (100) reflection plane, another at $2\theta \approx 6.0°$ ($q \approx 4.2$ nm^{-1}) attributed to the (210), and one at $2\theta \approx 26.1°$ ($q \approx 18.1$ nm^{-1}) for the (002) reflection plane. The two former reflection planes [(100) and (210)] are related to intralayer features, while (002) is related to interlayer ones. Quantum chemical computer models were applied to gain further insight into the molecular structure of the TpBD-Me$_2$ material. The diffraction pattern of the pristine sample was accurately reproduced from the simulations, allowing to identify its interlayer arrangement as hexagonal *AA* (Fig. 1), with the aromatic sheets aligned on top of each other in a graphitic fashion. The intralayer peaks are reproduced by the computer models, giving peaks at $2\theta = 3.39°$ and $5.89°$, attributed to (100) and (210) reflection planes, respectively.

The FTIR spectrum of pristine TpBD-Me$_2$ (Fig. S1a) demonstrates three strong bands at 1577, 1442, and 1247 cm^{-1}, which correspond to the C=C stretching and the aromatic C=C and C–N bonds, respectively. The Raman spectrum (Fig. S1b) features peaks within the spectral window from 950 to 1900 cm^{-1}, corresponding to the intramolecular
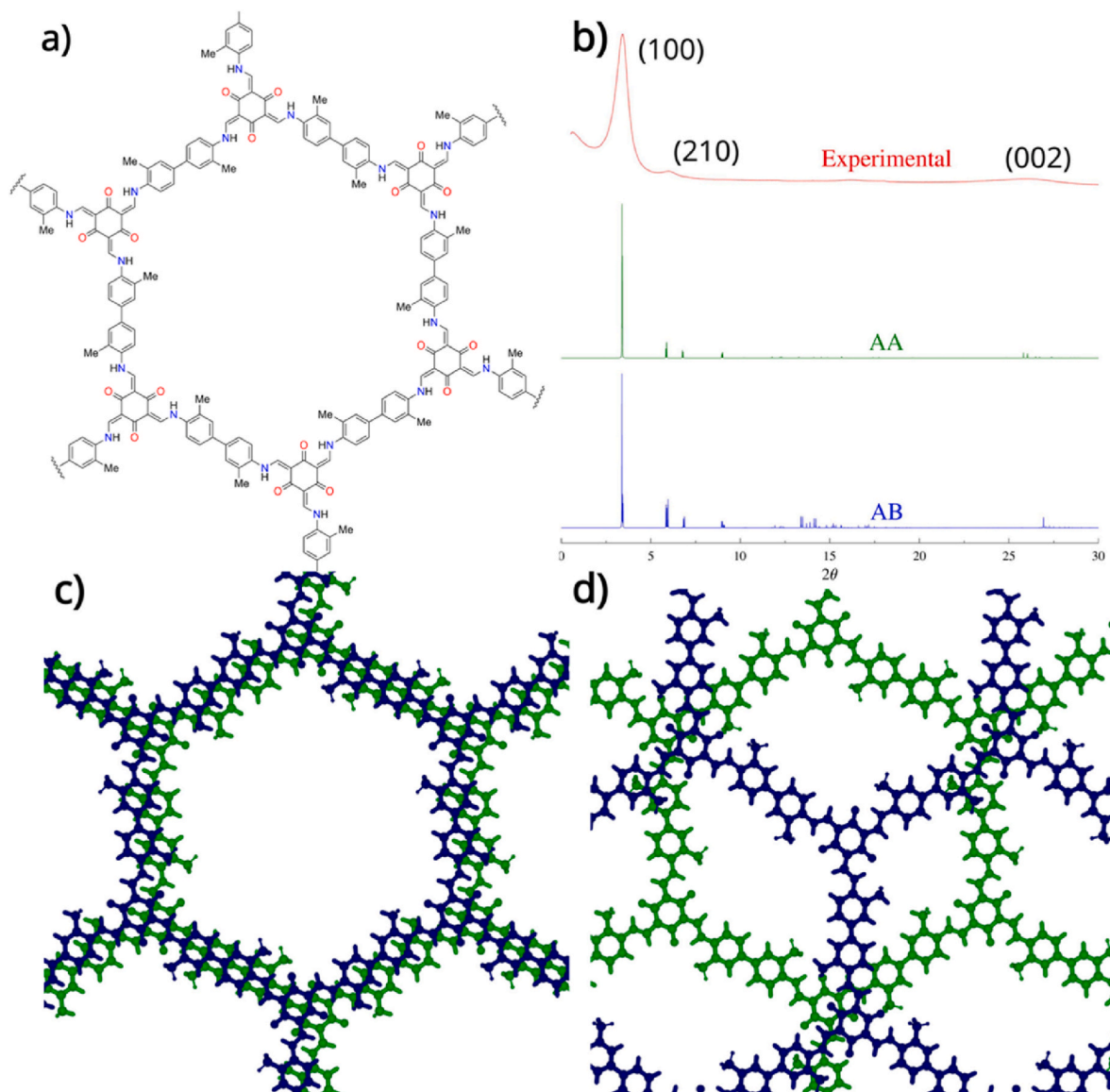
Fig. 1. Chemical structure (a), comparison of the experimental XRD pattern of TpBD-Me$_2$ with AA and AB computed structures (b), calculated AA (c) and AB (d) layer arrangements of the synthesized TpBD-Me$_2$.

modes, while the peaks within the spectral window from 190 to 700 cm^{-1} represent the translations and rotations of rigid molecules. In the high-frequency region of the Raman spectrum, one can observe the peaks centered at 1124 and 1605 cm^{-1}, corresponding to the C–N and C=N bonds formed by the reaction of the aldehyde and amine groups [22]. Pristine TpBD-Me$_2$ further exhibits a type I + II N$_2$ adsorption−desorption isotherm at 77 K (Fig. S1c), typical of materials presenting micropores and mesopores, with a specific surface area $S_{BET} = 423$ m^2 g^{-1}, determined by the BET method, matching well with the reported values for this type of COF [22]. Furthermore, pore size distribution estimated using quenched-solid density functional theory showed a large micropore contribution (Fig. S1c) and the presence of some small mesopores ($d < 10$ nm). Thermogravimetric analysis (TGA) of TpBD-Me$_2$ (Fig. S1d) under inert Ar atmosphere evidenced that the material did not lose mass until around 350 °C. A steep weight loss occurred at around 450 °C, after which the material gradually lost mass with increasing temperature, with 53% of total mass loss recorded at 900 °C.

To determine changes in crystallinity upon the different treatments, we measured the SAXS patterns of the treated COF samples and compared them with the pattern of the pristine COF (Fig. S2). The domain size (L) of pristine TpBD-Me$_2$ was determined using eq. (1), by fitting the SAXS pattern with eq. (2) (see the Experimental Section). This parameter directly correlates with the crystallinity of the material; therefore, a material with higher crystallinity presents a higher L value. The fitting is well adjusted to the data with $R^2 = 0.98$ (Fig. S3) giving a half width at half maximum (w) of 0.47 nm^{-1}, resulting in $L = 6.68$ nm, calculated using eq. (3).

The normalized SAXS patterns of the thermally treated samples (Fig. S2a) evidenced a decrease in the (100) intensity relative to the (002) reflection. Accordingly, a decrease in the domain size of the material was observed with increasing temperature (Table S1, Fig. S3a): when the material was subjected to annealing at 150 °C, the domain size of TpBD-Me$_2$ was nearly maintained with $L = 6.54$ nm, whereas increasing the temperature to 200 °C led to a minor decrease in domain size to $L = 6.04$ nm, followed by a much more accentuated decrease at 250 °C to $L = 2.47$ nm, with nearly complete loss in long-range structural order. Contrary to what was observed in the thermal stability testing, under the hydrothermal conditions tested the SAXS study indicated that the crystallinity of the COF remains nearly intact, with little difference

observed in the intensity of the (100) reflection relative to the (002) one after the treatments (Table S1). In fact, an opposite trend in the domain size was observed as compared to the thermal stability testing: an increase in L was found with increasing temperature, reaching a value of 7.31 nm for hydrothermally treated COF at 200 °C (Table S1). On the other hand, as in the case of thermal treatments, high mechanical pressure to form pellets resulted in a decrease in L (Table S1) with increasing mechanical force (Fig. S3c). In the SEM images (Fig. S4), the granular features of the as-synthesized TpBD-Me$_2$ seem largely conserved after the hydrothermal treatments. However, after thermal treatment and more clearly after mechanical pressure treatment there is

an evident loss of granularity.

The FTIR spectra acquired after all the treatments (Fig. S5) presented no changes in the peak positions. In the Raman spectra after the thermal treatment, however, clear variations in the background were found after annealing at 200 and 250 °C (Fig. 2k, S6a), with the Raman fingerprint of the COF disappearing almost completely in the sample heated at 250 °C.

For the samples after hydrothermal treatment, similar variations in the background intensity were found at 200 °C and somewhat also at 150 °C (Fig. 2k, S6b), although not as pronounced or homogeneous as in the case of the thermally treated samples. In addition, the Raman
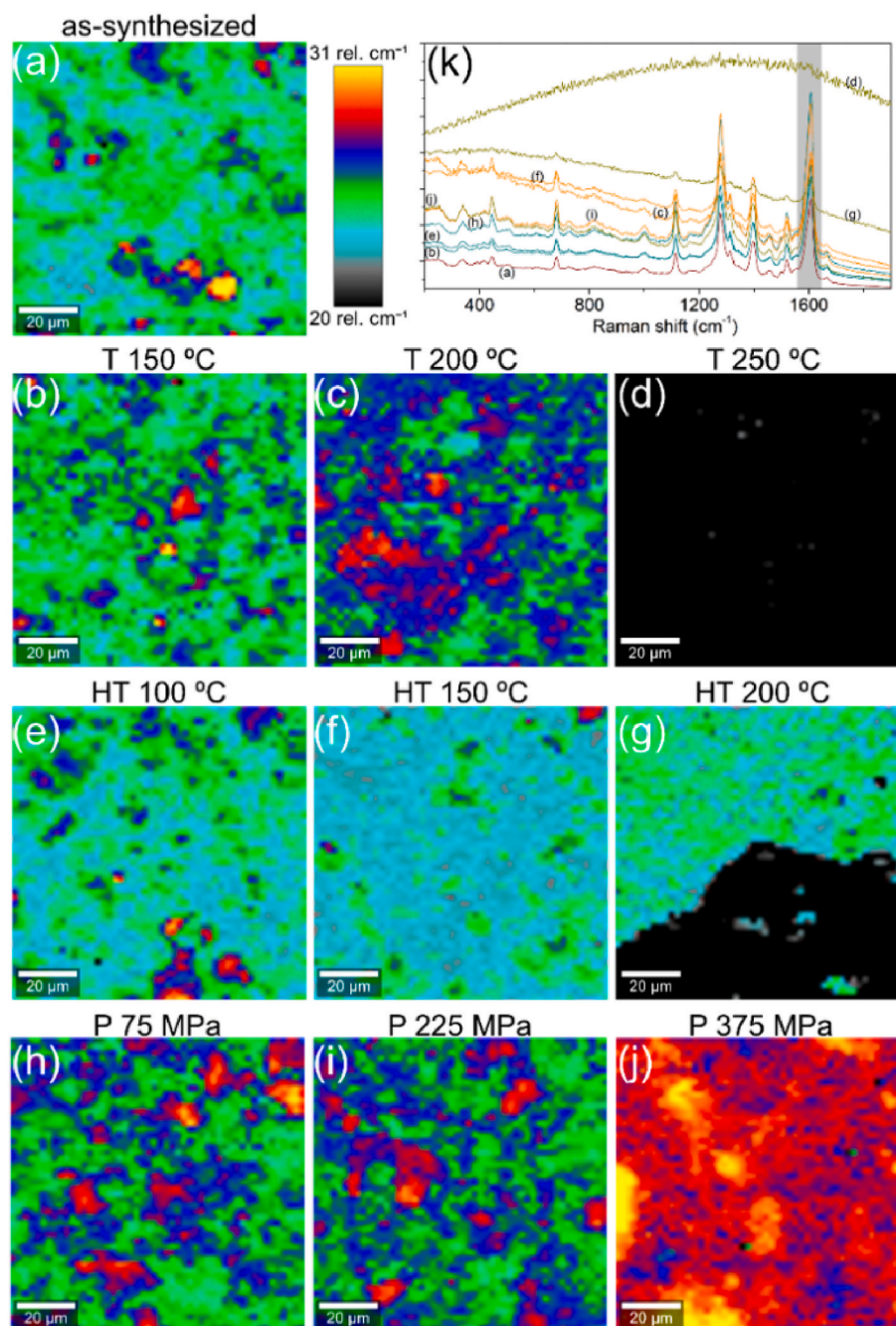

Fig. 2. Raman spectroscopy maps of TpBD-Me$_2$ (a) pristine and after (b–d) annealing at 150 °C (b), 200 °C (c), and 250 °C (d), (e–g) hydrothermal treatment at 100 °C (e), 150 °C (f), and 200 °C (g), and (h–j) mechanical pressure application with 75 MPa (h), 225 MPa (i), and 375 MPa (j). The Raman spectroscopy maps were acquired upon excitation with a 785 nm laser line and a spectral window centered at 1607 cm^{-1}, one of the characteristic peaks of TpBD-Me$_2$ [light gray rectangle in (k) to identify the variation on the full width at half maximum. The black area in the (d) and (g) Raman spectroscopy maps is due to the absence of the representative spectra of COF.

fingerprint of the COF disappeared partially in the sample treated hydrothermally at 200 °C (Fig. 2g). After exposing TpBD-Me$_2$ to mechanical pressure, a slight increase in the background of the Raman spectra was found with the sample treated at 375 MPa (Fig. 2k, S6c). Interestingly, an increase in the broadness of the peak centered at 1607 cm^{-1} was also clearly identified (Fig. 2j, S6f). After treatment at lower pressures of 75 and 225 MPa, a slight and non-homogeneous increase in the broadness was also observed (Fig. 2h,i, S6f).

N$_2$ adsorption−desorption isotherms at 77 K of the stability-tested samples were then measured. A significant loss of 78% in the S_{BET} was observed for the thermally treated sample already at 150 °C (S_{BET} = 93 m^2 g^{-1}), accompanied by a decrease in V_P from 0.35 to 0.12 cm^3 g^{-1}, and a slight increase in d_P from 1.1 to 1.5 nm (Table S1, Fig. 3a). After treatment at 200 °C, the surface area loss increased to 85 % (S_{BET} = 61 m^2 g^{-1}). A further increase in temperature to 250 °C additionally led to a significant increase in d_P to 4.5 nm. The pore size distribution (Fig. S7a) indicated that with increasing temperature, a decrease in the amount of micropores (<2 nm) occurs until they are completely lost after treatment at 250 °C, where only mesopores remain. Upon hydrothermal treatment at autogenous pressure (Table S1, Fig. 3b), the materials showed a much less significant decrease in S_{BET} as compared to that found after the annealing. Conversely, V_{micro} of the material increased under these conditions, while V_P remained the same. Notably, hydrothermal treatment at 100 °C produced a slight increase in S_{BET} to 480 m^2 g^{-1} as compared to the as-synthesized COF with S_{BET} = 423 m^2 g^{-1}. However, further increase in the temperature reversed the trend, with a loss of 7% to S_{BET} = 393 m^2 g^{-1} found after treatment at 200 °C as compared to the pristine material. The pore size maintained at d_P = 1.1 nm, increasing slightly to d_P = 1.6 nm after hydrothermal treatment at 200 °C.

Mechanical pressure also caused significant losses in the S_{BET} of the COF (Fig. 3c). Specifically, after applying 75 MPa of pressure to the COF with a hydraulic press, the formed pellet featured S_{BET} = 163 m^2 g^{-1}, 61% lower than that of the pristine material. A further increase in the applied pressure to 375 MPa led to a loss of 87% of the surface area (S_{BET} = 53 m^2 g^{-1}), accompanied by a loss in V_P to 0.07 cm^3 g^{-1}, and a complete loss of V_{micro} (Table S1, Fig. S7c). In this case, d_P shows an increase to 4.2 nm already at 225 MPa.

The XPS C 1s (Figs. S8, S9, S10) spectrum of as-synthesized TpBD-Me$_2$ was fitted with three components corresponding to (aromatic) C−C at binding energy (BE) 284.5 eV, a combination of C−N, C−O, C−CO at 285.7 ± 0.1 eV, C=O at 287.7 ± 0.3 eV, and also a broad component at 290.4 ± 0.7 eV corresponding to the aromatic π–π* shakeup feature.

Regarding the O 1s spectra, the peak observed at 530.7 ± 0.1 eV is related to the oxygen signal from C=O moieties in the COF. In the N 1s spectra, it is possible to observe a single primary peak at 399.7 ± 0.1 eV and two broad shakeup features at 402.5 ± 0.3 eV and 405.2 ± 0.3 eV [8,38].

Observing the XPS C 1s and N 1s spectra of the hydrothermally and mechanical pressure treated samples, no major chemical degradation (e. g., ring opening, oxidation, bond cleavage) seemed to occur, since the changes in the aromatic C–C and the imine N 1s peaks across all the samples are minimal. However, in the case of the thermally treated sample at 250 °C, the C 1s and N 1s spectra suggest that the COF suffers degradation to an extent in the lateral chemical structure and ordering, which is evident by the loss of the shake up features in both spectra [8, 38].

3.3. Computational modelling

An extensive search of various possible interlayer rearrangements of the bulk COF material was performed with quantum chemical methods. To understand the high-pressure modifications, we initially simulated the effect of TpBD-Me$_2$ compression with Molecular Dynamics (MD), which revealed that TpBD-Me$_2$ monolayers are quite pliable in nature, buckling considerably under pressure albeit with an energy penalty (see the SD for more details).

For the bulk COF, several interlayer arrangements were subsequently investigated. Among those, the hexagonal *AA* interlayer arrangement was predicted to show high thermodynamic stability with a binding energy of 2.9 eV per layer/unit cell, which is almost twice the value of the *AB* arrangement, 1.46 eV. In addition, *AA* matches very well the experimental XRD pattern (Fig. 1) and also featured the lowest density, 0.58 g cm^{-3}, and consequently shows the largest porosity when compared to other possible structures that showed competing and even marginally better binding energies, yet failed to match the experimental XRD pattern (Fig. S12).

Therefore, the structure of the as-synthesized TpBD-Me$_2$ was identified as *AA*, which, under various treatments transforms into other thermodynamically feasible arrangements such as inclined *AB* (Fig. 4, Table 1), which exhibits the largest density, 1.08 g cm^{-3}, and lowest total energy, and hence should be prevalent at high pressures. Furthermore, the transformation may plausibly go through the inclined *AA*, which is slightly denser than *AA* (0.64 g cm^{-3} cf. 0.58 g cm^{-3}) while preserving the characteristic large hexagonal pores. Relevantly, in both
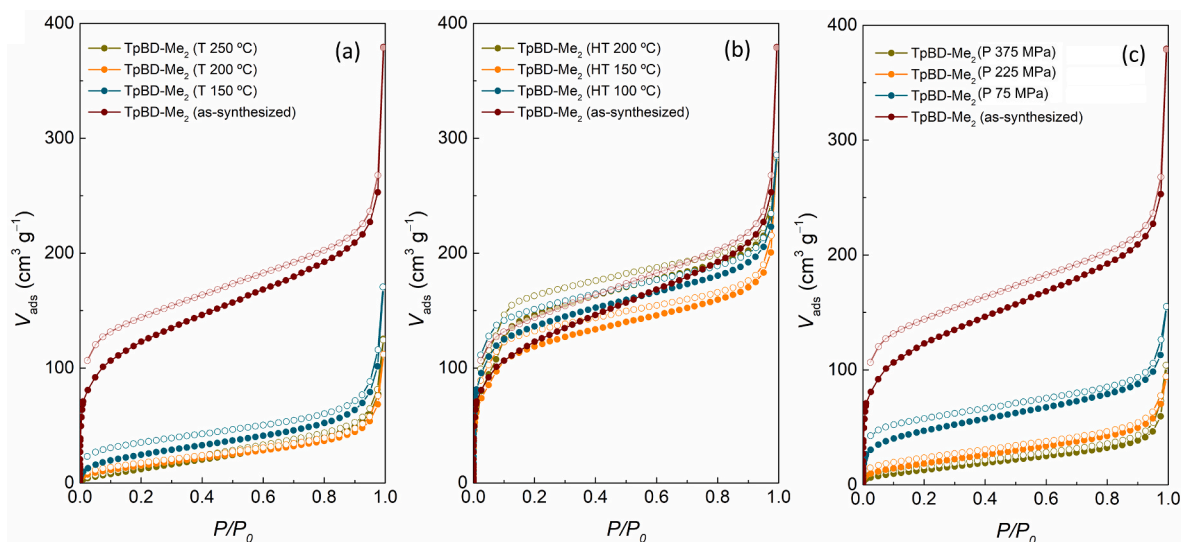

Fig. 3. N$_2$ adsorption−desorption isotherms recorded at 77 K of TpBD-Me$_2$ before and after (a) thermal treatment, (b) hydrothermal treatment, and after (c) applying mechanical pressure.
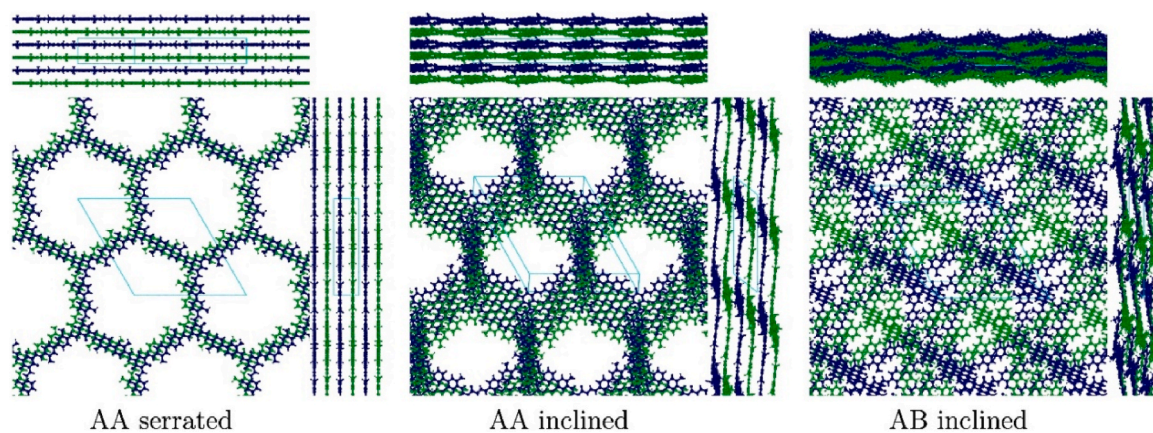
Fig. 4. Structures of AA (left) inclined AA (center) and inclined AB (right) unit cells of the TpBD-Me$_2$ COF at the PBE-MBD/light level.

Table 1

Properties of investigated interlayer arrangements of the TpBD-Me$_2$ COF, simulated at the PBE-MBD/light level of theory.

TpBD-Me$_2$ interlayer arrangement	Binding energy per layer (eV)	Density (g cm^{-3})	Pore limiting diameter (Å)	Pore accessible surface area (m^2 g^{-1})	Cell volume per layer (Å^3)
AA (pristine)	−2.885	0.58	19.3	1638	2702
AA inclined	−2.991	0.64	16.8	1663	2445
AB	−1.456	0.61	7.5	2111	2586
AB inclined	−3.023	1.08	6.6	1134	1456
Fully buckled	0.080	0.90	3.0	0	1743

inclined *AA* and inclined *AB* arrangements, the COF monolayers are buckled (Fig. 4), yet more stable as the energetic penalty of the out-of-plane distortion is compensated by more favorable interlayer interactions.

From the above results, the application of temperature or pressure will, likely and progressively, induce turbostratic disorder within the COF through different interlayer arrangements. Namely, under those conditions, the presence of regions with inclined *AA* and inclined *AB* layers mixed with *AA* arrangements, all with markedly different 2D unit cells (Table S2), will cause a decrease of accessible pore area, as the disorder due to mismatched heterogeneous stacking grows with increasing number of layers (Figs. S13 and S14).

4. Discussion

The stability of the three-dimensional structure of 2D COFs is not dependent only on the covalent bonds within the layer but also on non-covalent interlayer forces, dominated by dispersion interactions [39]. Conversely, charge repulsions between the heteroatoms of the COF layers can destabilize the structure [40]. Therefore, the two main pathways of degradation of the COF 3D structure are the breakage of covalent bonds or full delamination of the 2D layers. Interestingly, computational calculations have shown that 2D COF structures exhibit considerable disorder in the third dimension, with even the rare *ABC* stacking mode playing a role in the structure of some materials [41].

To systematically study the stability of TpBD-Me$_2$ COF under catalytically relevant conditions, the pristine material was subjected to thermal, hydrothermal, and mechanical pressure treatment and fully characterized both prior to and after the treatment. As indicated by the comparison of the domain size *L* derived from the SAXS patterns, TpBD-Me$_2$ initially seemed to be stable during annealing up to 200 °C, under all studied hydrothermal conditions, as well as under mechanical pressure with merely a slight reduction in *L* up to 225 MPa. FTIR confirmed that under all conditions studied, the covalent bonds of the material

remained intact.

Raman spectroscopy can give information about the degree of crystallinity of a solid material, and crystalline and amorphous solids with the same chemical composition can display significant differences in terms of variation of intensity, shift, or broadness. Specifically in organic crystals, the Raman peak variations can be interpreted and correlated with perturbations in terms of intermolecular interactions [42], rendering this method an interesting choice for the study of the stability of our COF materials.

Indeed, the Raman spectra of the COF materials evidenced differences after the treatments. As indicated by the Raman spectra after thermal treatment, TpBD-Me$_2$ underwent a direct solid-to-solid phase transition from crystalline to amorphous phase with increasing the temperature. Crystalline polymers have been reported to exhibit such phase transitions by changing the external conditions [43]. The observed increase in the background of treated TpBD-Me$_2$ can be attributed to an increase in the disorder, as reported by Saerens and co-workers [44] for glassy solid-solution of celecoxib in a polymeric matrix. Previously Raman spectroscopy has been used to observe the partial amorphization and collapse of the COF-1 structure when subjected to high pressures (>12−15 GPa) [45]. This pressure range was found to produce large changes in the intermolecular distances, provoking a change in the solid symmetry and a thus more evident modification in the Raman spectrum. In the TpBD-Me$_2$ COF after mechanical pressure treatment, a slight modification in both background and broadness of the characteristic COF peaks in the Raman spectra was observed, as expected due to the effect of pressure, resulting in a decrease in the intermolecular distances, while the interatomic separation of each molecule should undergo only a slight decrease. This means that the crystal symmetry should remain similar [46].

The greatest changes induced by the treatments were observed in the N$_2$ physisorption experiments. Dramatic losses in S_{BET} were observed already after thermal treatment at 150 °C even though SAXS and FTIR results indicated the materials to maintain their structural integrity under these conditions, and TGA indicated TpBD-Me$_2$ to be stable up to 350 °C under inert atmosphere. Notably, under hydrothermal treatment the surface area of TpBD-Me$_2$ was found to be preserved under all conditions studied. A slight increase in S_{BET} was even found after treatment at 100 °C, which could stem from removal of residual solvent guest molecules during the hydrothermal treatment that were not completely removed during the purification procedure of the pristine COF. The removal of these molecules thus decreased the network disorder, increased the crystallinity, and made more available vacant COF micropores, resulting in an increase of the V_{micro}. On the other hand, as seen with thermal treatment, mechanical pressure treatment, already at 75 MPa, led to a loss of S_{BET} of over 60%. The application of mechanical pressure has been previously shown to lead to decreases in the domain

sizes in boronic-acid-based COFs and a β-ketoenamine COF [47].

The radar chart (Fig. 5a) plotting the surface area S_{BET} and the domain size L for the conditions studied herein illustrates the obtained results. Namely, while hydrothermal conditions are seen to largely maintain the properties of the pristine COF, it is evident that both thermal and mechanical pressure treatments are detrimental to the surface area of the material.

The calculations indicated that the changes observed in the case of thermal and mechanical pressure treatments are likely related to arbitrary displacement or buckling of the 2D layers caused by the increase in the applied pressure or the temperature. Both the arbitrary displacement and the buckling of the layers are possible causes for the overall loss in crystallinity and the associated loss in S_{BET} and increase in the contribution of mesopores when the COF is heated under inert atmosphere or treated with mechanical pressure. In our calculations, the as-synthesized *AA* interlayer arrangement showed the lowest density. In comparison, the modelled inclined *AA* system, with a nearly equivalent thermodynamic stability, was found to be 19% more dense and should be more stable under pressure. The serrated *AB* interlayer arrangement showed a noticeable penalty in energy and should not be quantitatively populated. Interestingly, the inclined *AB* arrangement yielded both, the most thermodynamically stable and the densest bulk structure of TpBD-Me$_2$, surpassing the buckled structure induced by compression and nearly doubling the density of the pristine *AA* structure. These findings indicate that after the initial *AA* serrated arrangement, there is likely a plethora of different energetically feasible interlayer arrangements that can be accessed with the application of pressure or temperature (Fig. 5b). Furthermore, considering this, the experimentally observed reduction in porosity is related to extensive interlayer disorder, which in turn produces the closure of the pores (Fig. S13).

Buckling of COF layers has previously been observed by Dichtel and co-workers [48], who studied the thermal stability of an imine and a β-ketoenamine linked COF using *in situ* XRD upon heating. Interestingly, TpBD, which is a COF prepared from Tp and benzidine (BD), structurally very similar to the COF in our study, showed a significant mass loss at $T_{XRD} = 540$ °C, whereas we found large changes in the domain size already after treatment at 250 °C. This may be related to the longer duration of the heat treatment in our study, but also to the fact that the methyl substituent in TpBD-Me$_2$ could restrict the rotational freedom of the biphenyl moiety as compared to non-substituted BD. Rotation has been proposed to allow for the relaxation of thermally induced stress in COF structures, thus preventing layer buckling from occurring [49]. Interestingly, Lotsch and co-workers also observed temperature-induced phase transitions at lower temperatures with their large-pore imine COFs [50], when studied by *in situ* XRD upon heating at temperatures from 30 to 200 °C using a heating period of 4 h until measurement. Some of the materials showed structural changes already above 120 °C as seen through broadening of 002 stacking reflection, attributed to a transition

from *AA*-type to *AB*-type structure. This broadening was also seen in our results with TpBD-Me$_2$, in agreement with displacement of the 2D layers as indicated by calculations. However, except for the sample treated thermally at 250 °C, no shifts in the 100 reflections were found in our study, indicating that should layer buckling occur in TpBD-Me$_2$, it does not seem to prevail once the temperature decreases, and arbitrary displacement of the 2D layers seems to be the origin of the loss in order.

Finally, to gain insight into the effect of the structural changes of TpBD-Me$_2$ on the performance, we tested the as-synthesized COF and a representative sample after thermal, hydrothermal, and mechanical pressure treatment in liquid-phase hydrogenation of bromate as a model catalytic reaction (Fig. S17). In our previous work [51], we demonstrated TpBD-Me$_2$ COF to present considerable catalytic activity for bromate reduction. Interestingly, no significant differences in catalytic activity could be observed before and after the different treatments, with all the samples presenting similar BrO_3^- conversions, achieving a maximum of around 80%. This indicates that the surface area of the catalyst does not play a major role in the catalytic activity in the case of this model reaction. However, in our previous work on formic acid dehydrogenation [8], deactivation of the RuO$_2$ catalyst supported on TpBD-Me$_2$ was found at temperatures above 120 °C. Notably, even at 120 °C, the activity and crystallinity of the COF was found to decrease after 25 h. As a result of the study described herein, we were able to propose this decrease in activity to stem from the loss in specific surface area of the COF, originating from extensive interlayer disorder caused by the temperature, eventually resulting in the closure of the pores. Further, this phenomenon could possibly lead to the agglomeration/growth of the RuO$_2$ nanoparticles and be the cause of deactivation. To overcome this issue and increase COF stability under catalytic conditions, it is of interest to consider strategies that enhance the interlayer interactions in COFs [40], or allow for rotational freedom to compensate for the induced stress during catalysis [49].

5. Conclusions

In summary, we have studied the stability of β-ketoenamine TpBD-Me$_2$ COF under catalytically relevant conditions: thermal, hydrothermal, and mechanical pressure treatments. The pristine and treated COF materials were systematically characterized to gain insight into the possible structural changes under these conditions. The COF was found to largely maintain its structural integrity during hydrothermal treatment, pointing towards the applicability of this class of COFs under aqueous/steam conditions. Interestingly, both thermal treatment and mechanical pressure caused losses in surface area already at the lowest temperature and pressure studied. Computer models revealed that these changes arise from increasing interlayer disorder promoted by the layer buckling caused by these treatments, indicating that the design of COFs for application under such conditions should consider strategies that
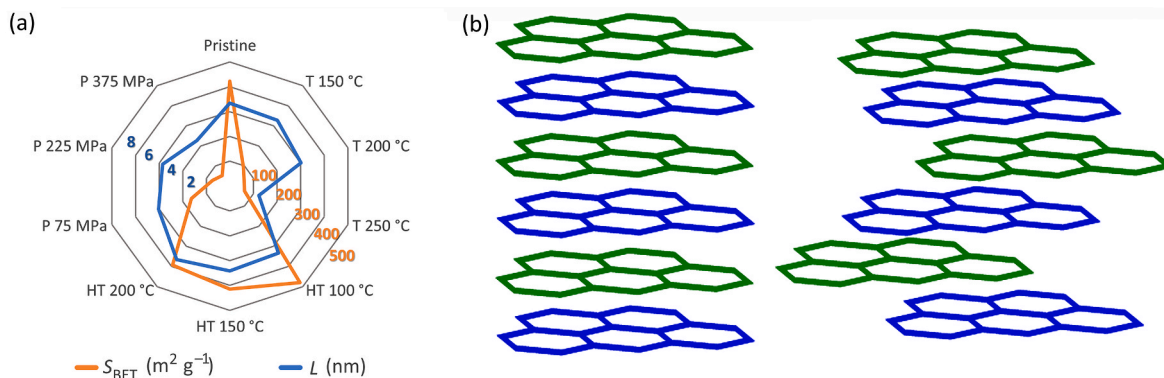

Fig. 5. Radar chart highlighting the influence of the treatment on the domain size L and the specific surface area S_{BET} (a), together with a scheme illustrating the COF layer arrangement after hydrothermal treatment (b, left) and thermal or mechanical pressure treatments (b, right).

enhance interlayer interactions and alleviate induced stress.

CRediT authorship contribution statement

Liliana P.L. Gonçalves: Writing – original draft, Visualization, Investigation, Formal analysis, Data curation. **Javier Garcia Ben:** Investigation, Formal analysis. **Karol Strutyński:** Visualization, Investigation, Formal analysis, Data curation. **Laura Rodriguez-Lorenzo:** Writing – original draft, Visualization, Methodology, Investigation, Formal analysis. **Joana Araújo:** Investigation. **A.Sofia G.G. Santos:** Investigation. **O. Salomé G.P. Soares:** Writing – review & editing, Supervision, Methodology. **M. Fernando R. Pereira:** Writing – review & editing, Supervision, Funding acquisition. **Yury V. Kolen'ko:** Writing – review & editing, Supervision, Funding acquisition, Conceptualization. **Manuel Melle-Franco:** Writing – original draft, Supervision, Methodology, Investigation, Funding acquisition, Formal analysis. **Laura M. Salonen:** Writing – review & editing, Supervision, Methodology, Funding acquisition, Conceptualization.

Declaration of competing interest

The authors declare that they have no known competing financial interests or personal relationships that could have appeared to influence the work reported in this paper.

Data availability

Data will be made available on request.

Acknowledgements

Appendix A. Supplementary data

Supplementary data to this article can be found online at https://doi.org/10.1016/j.micromeso.2023.112916.

References

[1] P. Munnik, P.E. de Jongh, K.P. de Jong, Recent developments in the synthesis of supported catalysts, Chem. Rev. 115 (2015) 6687–6718, https://doi.org/10.1021/cr500486u.

[2] M.S. Lohse, T. Bein, Covalent organic frameworks: structures, synthesis, and applications, Adv. Funct. Mater. 28 (2018), 1705553, https://doi.org/10.1002/adfm.201705553.

[3] S. Kandambeth, K. Dey, R. Banerjee, Covalent organic frameworks: chemistry beyond the structure, J. Am. Chem. Soc. 141 (2019) 1807–1822, https://doi.org/10.1021/jacs.8b10334.

[4] C.S. Diercks, O.M. Yaghi, The atom, the molecule, and the covalent organic framework, Science 355 (2017) 923, https://doi.org/10.1126/science.aal1585.

[5] H. Wang, Y. Yang, X. Liang Teo, Y. Wu, L. Tang, Y. Zhao, Structure–performance correlation guided applications of covalent organic frameworks, Mater. Today 53 (2022) 106–133, https://doi.org/10.1016/j.mattod.2022.02.001.

[6] J.J. Jarju, A.M. Díez, L. Frey, V. Sousa, E. Carbó-Argibay, L.P.L. Gonçalves, D. D. Medina, O.I. Lebedev, Y.V. Kolen'ko, L.M. Salonen, Synthetic strategy for metallophthalocyanine covalent organic frameworks for electrochemical water oxidation, Mater. Today Chem. 26 (2022), 101032, https://doi.org/10.1016/j.mtchem.2022.101032.

[7] S.Y. Ding, J. Gao, Q. Wang, Y. Zhang, W.G. Song, C.Y. Su, W. Wang, Construction of covalent organic framework for catalysis: Pd/COF-LZU1 in Suzuki-Miyaura coupling reaction, J. Am. Chem. Soc. 133 (2011) 19816–19822, https://doi.org/10.1021/ja206846p.

[8] L.P.L. Gonçalves, D.B. Christensen, M. Meledina, L.M. Salonen, D.Y. Petrovykh, E. Carbó-Argibay, J.P.S. Sousa, O.S.G.P. Soares, M.F.R. Pereira, S. Kegnæs, Y. V. Kolen'ko, Selective formic acid dehydrogenation at low temperature over a RuO₂/COF pre-catalyst synthesized on the gram scale, Catal. Sci. Technol. 10 (2020) 1991–1995, https://doi.org/10.1039/d0cy00145g.

[9] G.J. Chen, X.B. Li, C.C. Zhao, H.C. Ma, J.L. Kan, Y. Bin Xin, C.X. Chen, Y. Bin Dong, Ru nanoparticles-loaded covalent organic framework for solvent-free one-pot tandem reactions in air, Inorg. Chem. 57 (2018) 2678–2685, https://doi.org/10.1021/acs.inorgchem.7b03077.

[10] S.M.J. Rogge, A. Bavykina, J. Hajek, H. Garcia, A.I. Olivos-Suarez, A. Sepúlveda-Escribano, A. Vimont, G. Clet, P. Bazin, F. Kapteijn, M. Daturi, E.V. Ramos-Fernandez, F.X.I. Llabrés Xamena, V. Van Speybroeck, J. Gascon, Metal-organic and covalent organic frameworks as single-site catalysts, Chem. Soc. Rev. 46 (2017) 3134–3184, https://doi.org/10.1039/c7cs00033b.

[11] W. Tu, Y. Xu, S. Yin, R. Xu, Rational design of catalytic centers in crystalline frameworks, Adv. Mater. 30 (2018) 1–29, https://doi.org/10.1002/adma.201707582.

[12] J. Guo, D. Jiang, Covalent organic frameworks for heterogeneous catalysis: principle, current status, and challenges, ACS Cent. Sci. 6 (2020) 869–879, https://doi.org/10.1021/acscentsci.0c00463.

[13] Q. Yang, M. Luo, K. Liu, H. Cao, H. Yan, Covalent organic frameworks for photocatalytic applications, Appl. Catal. B Environ. 276 (2020), 119174, https://doi.org/10.1016/j.apcatb.2020.119174.

[14] R.K. Sharma, P. Yadav, M. Yadav, R. Gupta, P. Rana, A. Srivastava, R. Zbořil, R. S. Varma, M. Antonietti, M.B. Gawande, Recent development of covalent organic frameworks (COFs): synthesis and catalytic (organic-electro-photo) applications, Mater. Horiz. 7 (2020) 411–454, https://doi.org/10.1039/C9MH00856J.

[15] Y. Zhi, Z. Wang, H.-L. Zhang, Q. Zhang, Recent progress in metal-free covalent organic frameworks as heterogeneous catalysts, Small 16 (2020), 2001070, https://doi.org/10.1002/smll.202001070.

[16] J. Liu, N. Wang, L. Ma, Recent advances in covalent organic frameworks for catalysis, Chem. Asian J. 15 (2020) 338–351, https://doi.org/10.1002/asia.201901527.

[17] H. Wang, C. Qian, J. Liu, Y. Zeng, D. Wang, W. Zhou, L. Gu, H. Wu, G. Liu, Y. Zhao, Integrating suitable linkage of covalent organic frameworks into covalently bridged inorganic/organic hybrids toward efficient photocatalysis, J. Am. Chem. Soc. 142 (2020) 4862–4871, https://doi.org/10.1021/jacs.0c00054.

[18] S. Daliran, A.R. Oveisi, Y. Peng, A. López-Magano, M. Khajeh, R. Mas-Ballesté, J. Alemán, R. Luque, H. Garcia, Metal–organic framework (MOF)- covalent-organic framework (COF)- and porous-organic polymers (POP)-catalyzed selective C–H bond activation and functionalization reactions, Chem. Soc. Rev. 51 (2022) 7810–7882, https://doi.org/10.1039/D1CS00976A.

[19] H. Salemi, M. Debruyne, V. Van Speybroeck, P. Van Der Voort, M. D'hooghe, C. V. Stevens, Covalent organic framework supported palladium catalysts, J. Mater. Chem. A 10 (2022) 20707–20729, https://doi.org/10.1039/d2ta05234b.

[20] M. Zhang, C. Lai, F. Xu, D. Huang, S. Liu, Y. Fu, L. Li, H. Yi, L. Qin, L. Chen, Atomically dispersed metal catalysts confined by covalent organic frameworks and their derivatives for electrochemical energy conversion and storage, Coord. Chem. Rev. 466 (2022), 214592, https://doi.org/10.1016/j.ccr.2022.214592.

[21] M. Sanchez-Fuente, J.L. Alonso-Gómez, L.M. Salonen, R. Mas-Ballesté, A. Moya, Chiral porous prganic frameworks: synthesis, chiroptical properties and asymmetric organocatalytic applications 13 (2023) 1042, https://doi.org/10.3390/catal13071042.

[22] S. Chandra, S. Kandambeth, B.P. Biswal, B. Lukose, S.M. Kunjir, M. Chaudhary, R. Babarao, T. Heine, R. Banerjee, Chemically stable multilayered covalent organic nanosheets from covalent organic frameworks via mechanical delamination, J. Am. Chem. Soc. 135 (2013) 17853–17861, https://doi.org/10.1021/ja408121p.

[23] A. Mellah, S.P.S. Fernandes, R. Rodríguez, J. Otero, J. Paz, J. Cruces, D.D. Medina, H. Djamila, B. Espiña, L.M. Salonen, Adsorption of pharmaceutical pollutants from water using covalent organic frameworks, Chem. Eur. J. 24 (2018) 10601–10605, https://doi.org/10.1002/chem.201801649.

[24] J.H. Chong, M. Sauer, B.O. Patrick, M.J. MacLachlan, Highly stable keto-enamine salicylideneanilines, Org. Lett. 5 (2003) 3823–3826, https://doi.org/10.1021/ol0352714.

[25] S. Grimme, C. Bannwarth, P. Shushkov, A robust and accurate tight-binding quantum chemical method for structures, vibrational frequencies, and noncovalent interactions of large molecular systems parametrized for all spd-block elements (Z

= 1–86), J. Chem. Theor. Comput. 13 (2017) 1989–2009, https://doi.org/10.1021/acs.jctc.7b00118.

[26] R. Rüger, M. Franchini, T. Trnka, A. Yakovlev, E. van Lenthe, P. Philipsen, T. van Vuren, B. Klumpers, T. Soini, AMS 2021.1, SCM, 2021. http://www.scm.com.

[27] M. Gaus, A. Goez, M. Elstner, Parametrization and benchmark of DFTB3 for organic molecules, J. Chem. Theor. Comput. 9 (2013) 338–354, https://doi.org/10.1021/ct300849w.

[28] E. Caldeweyher, C. Bannwarth, S. Grimme, Extension of the D3 dispersion coefficient model, J. Chem. Phys. 147 (2017), 34112, https://doi.org/10.1063/1.4993215.

[29] B. Aradi, B. Hourahine, T. Frauenheim, DFTB+, a sparse matrix-based implementation of the DFTB method, J. Phys. Chem. A 111 (2007) 5678–5684, https://doi.org/10.1021/jp070186p.

[30] V. Blum, R. Gehrke, F. Hanke, P. Havu, V. Havu, X. Ren, K. Reuter, M. Scheffler, Ab initio molecular simulations with numeric atom-centered orbitals, Comput. Phys. Commun. 180 (2009) 2175–2196, https://doi.org/10.1016/j.cpc.2009.06.022.

[31] A. Marek, V. Blum, R. Johanni, V. Havu, B. Lang, T. Auckenthaler, A. Heinecke, H.-J. Bungartz, H. Lederer, The ELPA library: scalable parallel eigenvalue solutions for electronic structure theory and computational science, J. Phys. Condens. Matter 26 (2014), 213201, https://doi.org/10.1088/0953-8984/26/21/213201.

[32] V.W. Yu, F. Corsetti, A. García, W.P. Huhn, M. Jacquelin, W. Jia, B. Lange, L. Lin, J. Lu, W. Mi, A. Seifitokaldani, Á. Vázquez-Mayagoitia, C. Yang, H. Yang, V. Blum, ELSI: a unified software interface for Kohn–Sham electronic structure solvers, Comput. Phys. Commun. 222 (2018) 267–285, https://doi.org/10.1016/j.cpc.2017.09.007.

[33] A. Tkatchenko, R.A. DiStasio, R. Car, M. Scheffler, Accurate and efficient method for many-body van der Waals interactions, Phys. Rev. Lett. 108 (2012), 236402, https://doi.org/10.1103/PhysRevLett.108.236402.

[34] A. Ambrosetti, A.M. Reilly, R.A. DiStasio, A. Tkatchenko, Long-range correlation energy calculated from coupled atomic response functions, J. Chem. Phys. 140 (2014) 18A508, https://doi.org/10.1063/1.4865104.

[35] L. Sarkisov, A. Harrison, Computational structure characterisation tools in application to ordered and disordered porous materials, Mol. Simulat. 37 (2011) 1248–1257, https://doi.org/10.1080/08927022.2011.592832.

[36] L. Sarkisov, R. Bueno-Perez, M. Sutharson, D. Fairen-Jimenez, Materials informatics with PoreBlazer v4.0 and the CSD MOF database, Chem. Mater. 32 (2020) 9849–9867, https://doi.org/10.1021/acs.chemmater.0c03575.

[37] B. Yeskendir, J.-P. Dacquin, Y. Lorgouilloux, C. Courtois, S. Royer, J. Dhainaut, From metal–organic framework powders to shaped solids: recent developments and challenges, Mater. Adv. 2 (2021) 7139–7186, https://doi.org/10.1039/D1MA00630D.

[38] E.H. Lock, D.Y. Petrovykh, P. Mack, T. Carney, R.G. White, S.G. Walton, R. F. Fernsler, Surface composition, chemistry, and structure of polystyrene modified by electron-beam-generated plasma, Langmuir 26 (2010) 8857–8868, https://doi.org/10.1021/la9046337.

[39] S.A. Ahmed, Q. Liao, Q. Shen, M. Muhammad, F. Ashraf, J. Zhou, C. Shi, P. Muhammad, S. Hanif, K. Xi, X. Xia, K. Wang, pH-dependent slipping and exfoliation of layered covalent organic framework, Chem. Eur J. 26 (2020) 12996–13001, https://doi.org/10.1002/chem.202000837.

[40] M. Martínez-Abadía, A. Mateo-Alonso, Structural approaches to control interlayer interactions in 2D covalent organic frameworks, Adv. Mater. 32 (2020), 2002366, https://doi.org/10.1002/adma.202002366.

[41] Y. Zhang, M. Položij, T. Heine, Statistical representation of stacking disorder in layered covalent organic frameworks, Chem. Mater. 34 (2022) 2376–2381, https://doi.org/10.1021/acs.chemmater.1c04365.

[42] M.K. Mishra, K. Mishra, S.A. Syed Asif, P. Manimunda, Structural analysis of elastically bent organic crystals using in situ indentation and micro-Raman spectroscopy, Chem. Commun. 53 (2017) 13035–13038, https://doi.org/10.1039/C7CC08071A.

[43] P.J. Ratri, K. Tashiro, Phase-transition behavior of a crystalline polymer near the melting point : case studies of the ferroelectric phase transition of poly (vinylidene fluoride) and the b-to-a transition of trans-1,4-polyisoprene, Polym. J. 45 (2013) 1107–1114, https://doi.org/10.1038/pj.2013.42.

[44] L. Saerens, D. Ghanam, C. Raemdonck, K. Francois, J. Manz, R. Krüger, S. Krüger, C. Vervaet, J. Paul, T. De Beer, In-line solid state prediction during pharmaceutical hot-melt extrusion in a 12 mm twin screw extruder using Raman spectroscopy, Eur. J. Pharm. Biopharm. 87 (2014) 606–615, https://doi.org/10.1016/j.ejpb.2014.03.002.

[45] J. Sun, A. Iakunkov, I.A. Baburin, B. Joseph, V. Palermo, A. V Talyzin, Covalent organic framework (COF-1) under high pressure, Angew. Chem. Int. Ed. 59 (2020) 1087–1092, https://doi.org/10.1002/anie.201907689.

[46] A.M.R. Teixeira, P.T.C. Freire, A.J.D. Moreno, J.M. Sasaki, A.P. Ayala, J. Mendes Filho, F.E.A. Melo, High-pressure Raman study of L-alanine crystal, Solid State Commun. 116 (2000) 405–409, https://doi.org/10.1016/S0038-1098(00)00342-2.

[47] D.A. Vazquez-molina, G.S. Mohammad-pour, C. Lee, M.W. Logan, X. Duan, J. K. Harper, F.J. Uribe-romo, Mechanically shaped two-dimensional covalent organic frameworks reveal crystallographic alignment and fast Li-ion conductivity, J. Am. Chem. Soc. 138 (2016) 9767–9770, https://doi.org/10.1021/jacs.6b05568.

[48] A.M. Evans, M.R. Ryder, N.C. Flanders, E. Vitaku, L.X. Chen, W.R. Dichtel, Buckling of two-dimensional covalent organic frameworks under thermal stress, Ind. Eng. Chem. Res. 58 (2019) 9883–9887, https://doi.org/10.1021/acs.iecr.9b01288.

[49] A.M. Evans, M.R. Ryder, W. Ji, M.J. Strauss, A.R. Corcos, E. Vitaku, N.C. Flanders, R.P. Bisbey, W.R. Dichtel, Trends in the thermal stability of two-dimensional covalent organic frameworks, Faraday Discuss 225 (2021) 226–240, https://doi.org/10.1039/D0FD00054J.

[50] S.T. Emmerling, R. Schuldt, S. Bette, L. Yao, R.E. Dinnebier, J. Kästner, B.V. Lotsch, Interlayer interactions as design tool for large-pore COFs, J. Am. Chem. Soc. 143 (2021) 15711–15722, https://doi.org/10.1021/jacs.1c06518.

[51] A.S.G.G. Santos, L.P.L. Gonçalves, C.A. Orge, Yu. V. Kolen'ko, L.M. Salonen, M.F. R. Pereira, O.S.G.P. Soares, Efficient liquid-phase hydrogenation of bromate over nanosized Pd catalysts supported on TpBD-Me$_2$ covalent organic framework, Catal. Today 418 (2023), 114074, https://doi.org/10.1016/j.cattod.2023.114074.